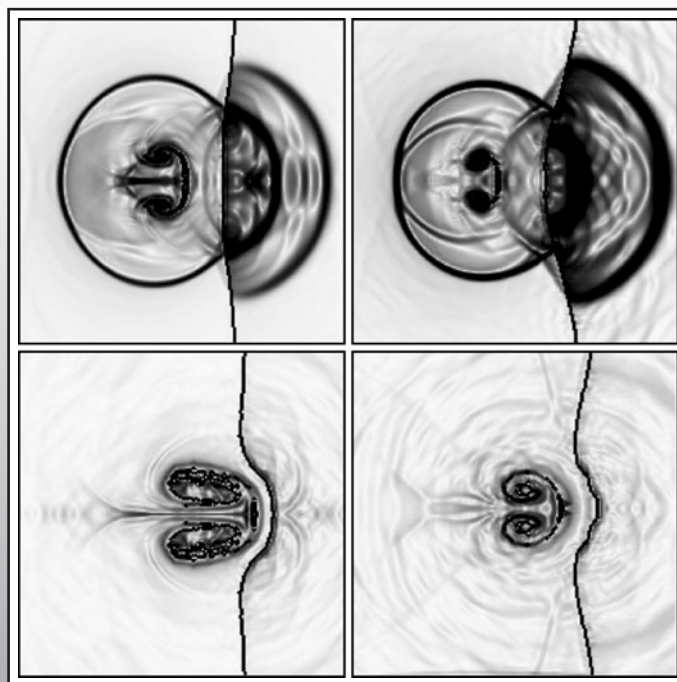


International Journal of
**Emerging
Multidisciplinary
Fluid Sciences**

Volume 1 · Number 2 · June 2009



Multi-Science Publishing
1756-8315

**©Multi-Science Publishing
2009**

International Journal of Emerging Multidisciplinary Fluid Sciences

Volume 1 · Number 2 · June 2009

Direct Numerical Simulations of Interaction of Strong Shock Waves with Nonspherical Gas Bubbles near Glass Boundaries in Mercury Hiroyuki Takahira, Kazumichi Kobayashi and Takahiro Matsuno	85
Integrated Experimental and Numerical Analysis of an Atmospheric Pressure Reactive Air Plasma Jet Generated by Dielectric Barrier Discharge Hideya Nishiyama, Hidemasa Takana, Hirofumi Shimizu, Yoshihiko Iwabuchi and Yoshikatsu Nakano	101
A Note on the Kinematics of Rigid Molecules in Linear Flow Fields and Kinetic Theory for Biaxial Liquid Crystal Polymers Jun Li, Sarthok Sircar and Qi Wang	115
Two-Dimensional Monte Carlo Simulations of Aggregation Phenomena in Ferromagnetic Colloidal Dispersions composed of Rod-like Hematite Particles Akira Satoh, Yasuhiro Sakuda and Yuta Katayama	127
Reduction of Drag Penalty by means of Plain Flaps in the Boomless Busemann Biplane Hiroshi Yamashita, Shigeru Obayashi and Kazuhiro Kusunose	141

Front Cover Window: Numerical schlieren images of bubble collapse in mercury (page 97)

Direct Numerical Simulations of Interaction of Strong Shock Waves with Nonspherical Gas Bubbles near Glass Boundaries in Mercury

Hiroyuki Takahira*, Kazumichi Kobayashi and Takahiro Matsuno
Department of Mechanical Engineering, Osaka Prefecture University,
1-1 Gakuen-cho, Naka-ku, Sakai, Osaka 599-8531, Japan
*E-mail: takahira@me.osakafu-u.ac.jp

ABSTRACT

The present study is concerned with the material damage of the liquid-mercury target systems induced by bubble collapse. The interaction of an incident strong shock wave with an initially spherical bubble near a glass wall in mercury is simulated using an improved Ghost Fluid Method (GFM), in which Riemann solutions are utilized to correct the values at boundary nodes. The mercury and glass are evaluated by using the equation of state for stiffened gas. The axi-symmetric motions of three phases for air, mercury, and glass are solved directly coupling the GFM with the level set method. The interaction of the shock wave with the bubble leads to the bubble deformation and the formation of liquid-jet during the collapse. The strong shock waves are generated in the mercury not only when the bubble rebounds but also when the liquid-jet impacts downstream surface of the bubble. It is shown that the impact of the shock waves on the glass wall leads to the formation of depression of the glass surface; the toroidal bubble formed after the impact of liquid-jet penetrates into the depression. The present results for the axi-symmetric bubble collapse are compared with those for the two-dimensional cylindrical bubble collapse. The stronger shock waves are generated when the axi-symmetric bubble collapses, which results in the higher impulsive pressure at the glass wall and the deeper depression of the glass surface.

Key Words: Bubble, Shock Wave, Mercury, Ghost Fluid Method, Riemann Solution

1. INTRODUCTION

The bubble collapse induced by shock waves in a liquid is a fundamental problem of bubble dynamics and cavitation, which must be clarified to understand phenomena such as material damage, noise, and performance drop of hydraulic machinery [1]. Nowadays, the study field for the bubble collapse extends in various fields of engineering, medicine, and physics. For example, in the medical applications, Extracorporeal Shock Wave Lithotripter (ESWL) has been widely used for urinary lithiasis. In ESWL, the shock waves generated outside of human body are utilized to crush the calculi in patients' body. When the calculi are crushed, however, cavitation bubbles are formed near the calculi. The cavitation bubbles cause tissue damages [2]. A cell permeabilization technique with shock waves induced by bubble collapse is also being developed in gene therapy and anticancer drug delivery [3]. Moreover, the material damage due to cavitation bubble collapse in liquid-mercury target systems for high-intense pulsed-spallation neutron sources is a big problem to be overcome in order to make a lifetime of the systems longer [4]. In the liquid mercury target system for MW-class neutron source installed in Japan Proton Accelerator Research Complex (J-PARC), high-intensity neutrons are produced by injecting MW pulsed proton beams from a high-intensity proton accelerator into the mercury target. Injecting the proton beams produces the pressure waves in the mercury due to rapidly deposited heat energy from the beams. The pressure waves interact with the vessel wall, which results in the generation of negative pressure leading to cavitation. The vessel wall is damaged by cavitation. To understand the phenomena, Futakawa et al. [4] performed the laboratory experiment for cavitation damage using a vessel with a glass wall. They showed that the cavitation damage is predicted by the

damage potential calculated from acoustic vibration caused by cavitation bubble collapse [4]. To reduce cavitation occurrence, the influence of injection of gas bubbles into liquid mercury has been studied [5, 6]. Okita et al. [5] showed numerically that when the initial void fraction is larger than the rate of thermal expansion of liquid mercury, the pressure rise caused by the thermal expansion decreases with decreasing the bubble radius, because of the increase of the natural frequency of bubbly mixture. Ida et al. [6] showed that the explosive expansion of cavitation nuclei is suppressed by the injection of gas bubbles because of bubble-bubble interactions. These studies are, however, based on the assumption of spherical bubbles. To understand the material damage in liquid mercury, the nonspherical bubble dynamics near a wall should be clarified. The mechanism of nonspherical bubble collapse in mercury, therefore, is a main concern in the present study. To understand the mechanism of nonspherical bubble collapse in mercury, Takahira et al. [7] simulated the collapse of a cylindrical bubble near a glass boundary induced by an incident shock wave using the Ghost Fluid Method (GFM) [8]. The motions of three phases for air, mercury, and glass were solved directly coupling the GFM with the level set method. They showed that the glass wall is deformed due to the shock waves generated by the bubble collapse, and the bubble takes a similar motion to that near a compliant wall. However, their results are restricted to the two-dimensional analysis. In the present study, an improved Ghost Fluid Method used in Takahira et al. [7] was applied to the problem for the interaction of an incident shock wave with an axi-symmetric bubble near a glass wall in mercury.

As is well known, in the numerical simulations of compressible two-phase flows with Eulerian schemes, special treatments are needed for the discontinuous variables at the interface because the discontinuity causes large truncation errors near the interface. In the GFM, the boundary conditions at the interface are captured implicitly by defining artificial fluid (Ghost Fluid) instead of explicitly applying Rankine-Hugoniot jump condition at the interface [8]. As a result, this method eliminates both dispersive and dissipative errors and captures the discontinuity at the interface accurately. However, one problem in applying the GFM with fully Eulerian schemes to the interfacial motion in which the one fluid is stiff (e.g., gas-liquid interface) is the pressure oscillations near the interface; the solution sometimes diverges due to the pressure oscillations [9]. For stiff fluids, therefore, to avoid the divergence, careful treatment is needed for the variables on both sides of the interface. Successful calculations were realized in Refs. [10, 11]. The front tracking method was used to capture the interface in Ref. [10], while the level set method was used in Ref. [11]. In both methods, the Riemann solutions at the interface were used to correct the values at boundary nodes in the Eulerian mesh. Takahira and Yuasa [12, 13] also used the Riemann solutions with the iterative algorithm to avoid pressure oscillations. This method is applied to the collapse of cylindrical air bubbles in mercury [7].

In the present work, the direct numerical simulations are performed for the collapse of an initially spherical air bubble near a glass wall in mercury induced by the interaction of the incident shock wave with the bubble in order to evaluate the material damage in the laboratory experiment by Futakawa et al. [4] for the liquid-mercury target systems. Although the vapor bubble collapse should be treated for the actual cavitation damage in the liquid-mercury target systems, the air bubble collapse is treated in the present study because the accurate treatment of phase change through the deformable interface is too complicated. However, the fundamental mechanism of material damage will be explained using the present simulation. The numerical technique used in Takahira et al. [7] is applied to the axi-symmetric collapse of the bubble. The influence of shock-bubble interaction on the glass wall is investigated for various bubble-wall distances. The difference between the two-dimensional and axi-symmetric simulations is also discussed.

2. NUMERICAL PROCEDURE

2.1 Euler Equations

The governing equations for the present analysis are Euler equations for the two-dimensional axi-symmetric compressible flow. The axi-symmetric Euler equations are given by

$$\frac{\partial Q}{\partial t} + \frac{\partial F}{\partial r} + \frac{\partial G}{\partial z} = S, \quad (1)$$

$$\mathbf{Q} = \begin{bmatrix} \rho \\ \rho u_r \\ \rho u_z \\ \hat{E} \end{bmatrix}, \quad \mathbf{F} = \begin{bmatrix} \rho u_r \\ p + \rho u_r^2 \\ \rho u_r u_z \\ (\hat{E} + p)u_r \end{bmatrix}, \quad \mathbf{G} = \begin{bmatrix} \rho u_z \\ \rho u_r u_z \\ p + \rho u_z^2 \\ (\hat{E} + p)u_z \end{bmatrix}, \quad \mathbf{S} = -\frac{1}{r} \begin{bmatrix} \rho u_r \\ \rho u_r^2 \\ \rho u_r u_z \\ (\hat{E} + p)u_r \end{bmatrix}, \quad (2)$$

where t is time, r and z are cylindrical coordinates, ρ is the density, u_r and u_z are velocities in the r and z directions, respectively, \hat{E} is the total energy per unit volume and p is the pressure. We use the following equation of state for stiffened gas [14]:

$$p = (\gamma - 1)\rho e - \gamma\Pi, \quad (3)$$

where e is the internal energy per unit mass, and γ and Π are parameters for the characteristic of materials [14]. For ideal gas, Π is zero and γ is taken to be the ratio of specific heat. For mercury and glass, γ and Π are determined so that the density and acoustic impedance agree with their physical properties. The acoustic impedance Z is defined as $Z = \rho a$ where $a = \sqrt{\gamma(p + \Pi)/\rho}$ is the speed of sound for the stiffened gas equation. The following γ and Π are utilized in the simulation:

$$\begin{aligned} \text{Air:} & \quad \gamma = 1.4, \Pi = 0 \text{ Pa}, \\ \text{Mercury:} & \quad \gamma = 8.2, \Pi = 35 \times 10^8 \text{ Pa}, \\ \text{Glass:} & \quad \gamma = 6.0, \Pi = 123 \times 10^8 \text{ Pa}. \end{aligned}$$

These values are the same as those used in Ref. [7].

In the present study, the stiffened gas equation is used for glass: the glass is treated as a compressible fluid. As shown in Ref. [15], under conditions of extremely high impulsive stress, the shock waves propagate in a material in a manner similar to the fluid dynamics situation. Thus the present treatment is valid when the very high pressure beyond the elastic limit is applied to the material. Therefore, the magnitude of the incident shock wave is taken to be of the order of GPa in the present study. Since the glass is treated as a compressible fluid and the strong shock waves impact the glass, the present numerical simulations correspond to the situations beyond the elastic limit.

The 3rd order TVD Runge-Kutta scheme and the 3rd order ENO-LLF scheme [16] are used for time and space discretization of eqn (1), respectively.

2.2 Level Set Method

The level set function, φ , is used to determine interface location. φ is the signed distance function from the interface. The location of the interface is defined as a set of points where $\varphi = 0$. Two kinds of fluid are distinguished by the sign of the level set function. φ is advanced by solving the following equation [17]:

$$\frac{\partial \varphi}{\partial t} + u_r \frac{\partial \varphi}{\partial r} + u_z \frac{\partial \varphi}{\partial z} = 0. \quad (4)$$

Since φ is diffused or distorted by the flow field, the reinitialization procedure is needed to maintain φ as a true distance function. The reinitialization equation is given by

$$\frac{\partial \varphi}{\partial \tau} + S(\varphi_0)(1 - |\nabla \varphi|) = 0, \quad (5)$$

where $S(\varphi_0) = \varphi_0 / \sqrt{\varphi_0^2 + h^2}$ is the sign function of φ_0 ($= \varphi(\tau = 0)$) with appropriate numerical smearing [17] and h is grid spacing. After solving eqn (4), eqn (5) is solved until it converges near the interface in fictitious time, τ .

Using the level set function, the unit normal at each grid point is defined as

$$\mathbf{n} = \frac{\nabla \varphi}{|\nabla \varphi|}. \quad (6)$$

We use the 3rd order TVD Runge-Kutta scheme and the 5th order WENO scheme [18] for time and space discretization of eqns (4) and (5), respectively. We also apply the hybrid particle level set method

developed by Enright et al. [19]. In this method, massless signed marker particles are passively advected along with the flow. The particles move according to $dx_p/dt = u(x_p)$ where $u(x_p)$ is the fluid velocity interpolated at the particle location x_p . The level set function is corrected with these particles. The correction using the particles are applied to both eqns (4) and (5). The hybrid particle level set method was designed to track material interfaces for both incompressible and compressible flows where characteristics are not created or destroyed. Therefore, applying the method to strong compressible flows where particles need to be created and destroyed in a consistent fashion to track characteristic information using marker particles may involve errors in tracking interfaces. However, as long as we applied the method to the problems for shock-bubble interactions in the previous works [12, 13], it worked well in conserving the mass of bubbles.

2.3 Ghost Fluid Method

In the GFM, ghost fluids are defined at every grid point in the computational domain so that each grid point contains the mass, momentum, and energy for real fluid that exists at that grid point, and a ghost mass, momentum and energy for the other fluid that does not really exist at that grid point [8]. For example, fluid 1 exists in the region where $\varphi < 0$, and fluid 2 exists in the region where $\varphi > 0$. Then artificial fluid for fluid 2 (ghost fluid 2) is defined in the region where $\varphi < 0$, and artificial fluid for fluid 1 (ghost fluid 1) is also defined in the region where $\varphi > 0$.

In the original GFM, the pressure and normal velocity of ghost fluid are copied over from the real fluid in a node by node fashion while the entropy and tangential velocity are defined with constant extrapolation in the normal direction. In the improved GFM [7, 12, 13], the definition of ghost values is modified as follows. For the ghost fluid of air, the pressure as well as entropy and tangential velocity are extrapolated from real air. For the ghost fluid of mercury, the normal velocity as well as entropy and tangential velocity are extrapolated from real mercury. For mercury-glass interface, we apply the original extrapolation procedure of the GFM. We use the fast extension method based on the Fast Marching Method for the extrapolation [20]. In the Fast Marching Method, a physical variable I to be extrapolated is determined by using the following equation:

$$\nabla\varphi \cdot \nabla I = 0. \quad (7)$$

The central difference is utilized to calculate spatial derivative in eqn (7). Once the ghost fluids are defined, we can use standard method for single-phase fluid to update Euler equations because there are two fluids respectively at every grid point in the computational domain. After updating Euler equations for each fluid separately, the level set function is utilized to decide which of the two fluids is valid at each grid point. The valid fluid is kept and the other is discarded so that only one fluid is defined at each grid point.

2.4 Boundary Treatment

The GFM with fully Eulerian schemes is effective in the computation of compressible flows with gas-gas interface. However, it is unstable in the computation of compressible flows with gas-liquid interface; unrealistic pressure oscillations occur near the interface and the solutions diverge [9]. This problem is caused by large sensitivity of the scheme to the numerical errors across the interface. To avoid this problem, the values on both sides of the interface are corrected by using the values at the neighboring nodes and the solution of the Riemann problem at the interface. Cocchi and Saurel [10] used the front tracking method and corrected the values on both sides of the interface using the solution of the Riemann problem following the normal at the interface. On the other hand, Nourgaliev et al. [11] used the level set method for interface capturing and corrected the values on both sides of the interface using the one-dimensional Riemann solution in each direction of the Cartesian coordinates with iterative algorithm. For one-dimensional problems, both methods are basically the same with each other. In the present simulations, we use the correction algorithm based on Nourgaliev et al. [11]. We correct the primitive variables on both sides of the interface with iterative algorithm for more than one-dimensional problems. The correction procedure follows [12, 13].

2.4.1 Correction of boundary nodes

First, we choose Boundary Nodes (BNs) at $t = t^n$ between which the interface exists. For example, if the sign of the level set function changes between the nodes (i, j) and $(i+1, j)$ in the two-dimensional domain, then the interface is located between the nodes. Thus the node (i, j) and $(i+1, j)$ are chosen as

BNs. Then we solve the one-dimensional Riemann problem between the nodes (i, j) and $(i+1, j)$ and determine the solutions at $t = t^{n+1}$ which are denoted as ψ_L^* and ψ_R^* at both sides of the interface where ψ represents the primitive variable u, p , or ρ [21]. Although the normal velocity and pressure at the interface are defined as one value because they are continuous across the interface, the density and tangential velocity are not defined as one value because they are discontinuous across the interface. The density of each fluid is defined by using the equation of state for each fluid. It should be noted that the Riemann solution for velocities is only defined in the normal direction. That is, the Riemann solution for the velocity in the y direction, v^* , is not defined along the grid line i in the x direction in Figure 1. Similarly, the Riemann solution for the velocity in the x direction, u^* , is not defined along the grid line j . For the tangential velocities, therefore, the Riemann solution v^* at each side of the interface is defined as $v_{i,j}$ at the node (i, j) for the left-hand side of the interface and $v_{i+1,j}$ at the node $(i+1, j)$ for the right-hand side of the interface, respectively, as shown in Figure 1. This definition is valid because the tangential velocity is the Riemann invariant along the normal direction [10]. Thus we can define all primitive variables on both sides of the interface.

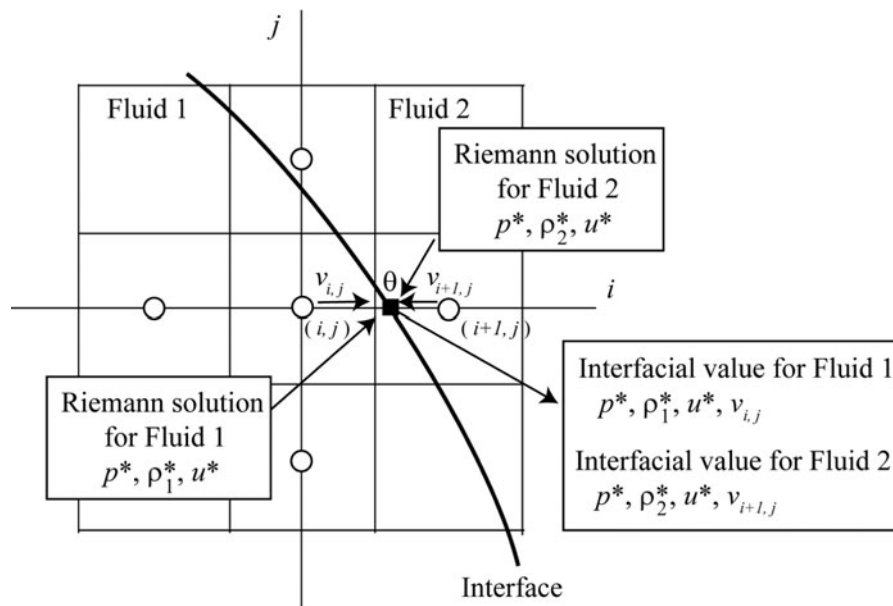


Figure 1. Determination of interfacial values.

The correction procedure for the one dimensional problem is explained below. Let us suppose the interface is located between the nodes i and $i+1$ at $t = t^n$ as shown in Figure 2. In Figure 2, u and a are the flow velocity and the speed of sound, respectively. The left-hand side and the right-hand side of the interface are fluid 1 and fluid 2, respectively. We will correct the primitive variables defined at the nodes i and $i+1$. First, we solve the one-dimensional Riemann problem between the nodes i and $i+1$ and determine the solutions ψ_L^* and ψ_R^* at both sides of the interface. Next, the level set function is updated, and the interface location at $t = t^{n+1}$ is determined. Then, the primitive variables are updated by solving the Euler equations. At each step of the TVD Runge-Kutta procedure for eqn (1), the primitive variables defined at the nodes i and $i+1$ are corrected. We define the following variable for interface location:

$$\theta^{n+1} = \frac{\varphi_i^{n+1}}{\varphi_i^{n+1} - \varphi_{i+1}^{n+1}}, \tag{8}$$

where φ_i^{n+1} is the level set function at $t = t^{n+1}$. If the interface is located between the nodes i and $i+1$ at $t = t^{n+1}$ as in Figure 2(A), θ^{n+1} lies between 0 and 1. While, if the interface moves beyond the node $i+1$ in the right direction (Figure 2(B)) or the node $i-1$ in the left direction (Figure 2(C)) during $\Delta t = t^{n+1} - t^n$, θ^{n+1} becomes greater than 1 or less than 0, respectively. Using θ^{n+1} , the correction of ψ_i^{n+1} and ψ_{i+1}^{n+1} is obtained from

$$\psi_i^{n+1} = \begin{cases} \psi_R^*, & \theta^{n+1} < 0, \\ \psi_{i-1}^{n+1} - \frac{\psi_{i-1}^{n+1} - \psi_L^*}{1 + \theta^{n+1}}, & \text{otherwise,} \end{cases} \quad (9)$$

$$\psi_{i+1}^{n+1} = \begin{cases} \psi_L^*, & \theta^{n+1} > 0, \\ \psi_{i+2}^{n+1} - \frac{\psi_{i+2}^{n+1} - \psi_R^*}{2 - \theta^{n+1}}, & \text{otherwise.} \end{cases} \quad (10)$$

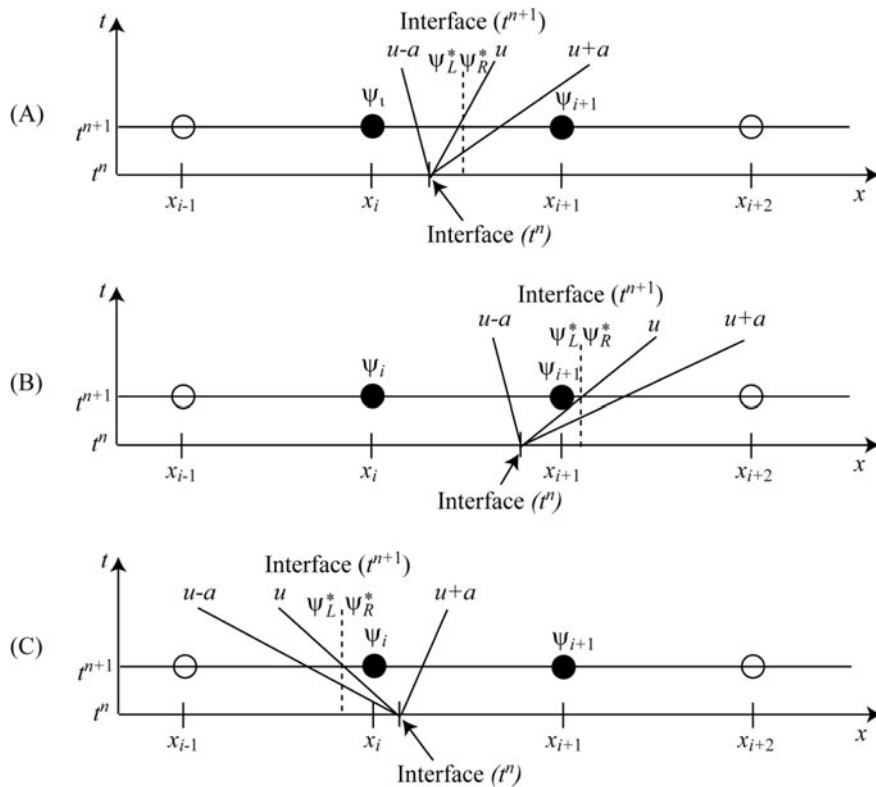


Figure 2. Correction of boundary nodes (one-dimension).

For two-dimensions, the following iteration procedure is utilized for correction. Let us consider the correction of values at the node P in Figure 3. We will consider four different interface locations (case (A-D)) in Figure 3. First, we store all current (m th) iteration values, $\psi^{(m)}$, on both sides of the interface. In case (A), the interface crosses the grid line i between the nodes E and EE in the x direction. In this case, since no interface is located between the nodes P and E , the primitive variables at the node P are corrected in the x direction as

$$\psi_{P(x)} = (\psi_E + \psi_W) / 2, \quad (11)$$

where subscript (x) denotes the correction in the x direction. In case (B), the interface crosses the grid line i between the nodes P and E in the x direction. In this case, ψ in the node P is corrected by using eqn (9). In case (C), the interface crosses the grid line i between the nodes W and P in the x direction. In this case, ψ in the node P is corrected by using eqn (10). In case (D), the interface crosses the grid line i both between the nodes P and E and the nodes P and W in the x direction. Letting $\psi_{L,1}^*$ and $\psi_{R,1}^*$ be the Riemann solutions on the left interface to the node P , and $\psi_{L,2}^*$ and $\psi_{R,2}^*$ be the Riemann solutions on the right interface to the node P , $\psi_{P(x)}$ is calculated from $\psi_{P(x)} = (\psi_{R,1}^* + \psi_{L,2}^*) / 2$. The above procedure

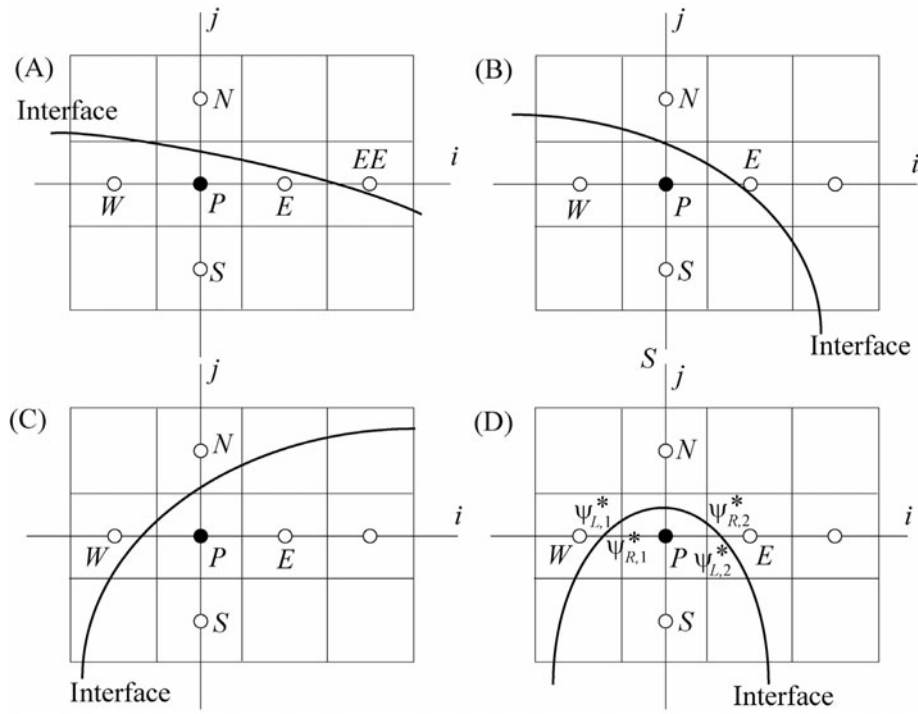


Figure 3. Correction of boundary nodes (two-dimension).

is also applied in the y direction and the correction $\psi_{P(y)}$ is obtained. Then, we define $\psi_P^{(m+1)}$ as

$$\psi_P^{(m+1)} = n_x^2 \psi_{P(x)} + n_y^2 \psi_{P(y)}, \quad (12)$$

where n_x and n_y are the component of unit normal at the node P in the x and y directions, respectively. We iterate these procedure until ψ_P converges for all boundary nodes. These procedures shown above are applicable to the analysis of the axi-symmetric Euler equations.

2.4.2 Treatment of motion of three phases

Since the experiments by Futakawa et al. [4] were done using the vessel with a glass wall, the bubble collapse near glass boundary is a target of the present analysis. To simulate bubble collapse in mercury near the glass wall, three kinds of material, i.e., air inside the bubble, mercury, and glass, should be distinguished. As shown in Figure 4, we define that the region where $\varphi < 0$ is for mercury. Thus the physical properties for mercury are utilized in the region where $\varphi < 0$. The region where $\varphi > 0$ is for air or glass. To distinguish air and glass, the glass region is determined by considering the deformation of the glass boundary as follows. We let the value of the z coordinate of the glass surface at time t be $z_g(r)$ in Figure 4. If the glass boundary $z_g(r)$ is located between the nodes (k, j) and $(k+1, j)$, then $\varphi_{k,j} \times \varphi_{k+1,j} < 0$. Thus we can seek the boundary nodes (k, j) and $(k+1, j)$. Letting the z coordinate of cell (k, j) be $z_{k,j}$, we take a reference value $z_{ref}(j)$ as $z_{ref}(j) = z_{k,j}$. Using $z_{ref}(j)$, the cells for glass domain are determined as $\varphi > 0$ and $z_{i,j} > z_{ref}(j)$. Similarly the cells for air domain are determined as $\varphi > 0$ and $z_{i,j} < z_{ref}(j)$. This choice does not allow the merger of air and glass. In the present code, at least two grid points are needed between the air-mercury and mercury-glass interfaces to calculate the Riemann solutions. Also as described above, $z_{ref}(j)$ is not allowed to have more than one value with respect to r . Thus, if the number of grid points between the air-mercury and mercury-glass interfaces becomes one or the glass surface deforms so that $z_{ref}(j)$ has more than one value, the calculation is forced to stop.

3. NUMERICAL RESULTS

The computational domain and bubble arrangement are shown in Figure 4. An initially spherical air bubble with the radius of R_0 is at rest near a glass wall. Following the analysis by Takahira et al. [7], R_0 is taken to be 3 mm in the present analysis. The distance between the bubble centroid and the glass

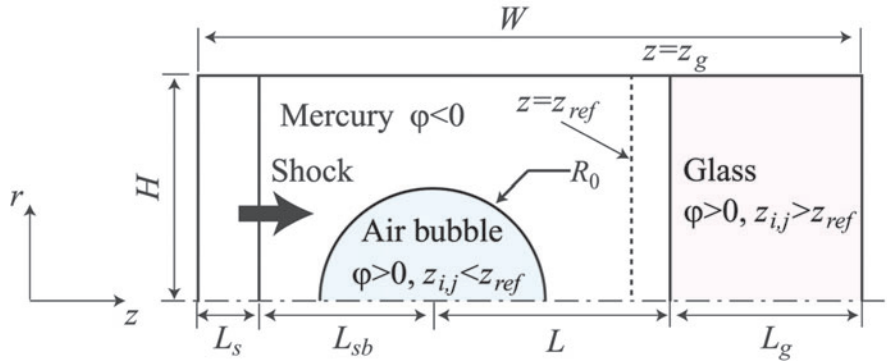


Figure 4. A schematic of computational domain.

wall is L . An incident shock wave propagates from the left-hand side of the bubble. The width and height of the computational domain are $W = 8R_0$ and $H = 4R_0$, respectively. The initial distance between the shock front and the bubble centroid is $L_{sb} = 1.4R_0$. The initial computational region behind the incident shock is $L_s = 2.6R_0$. The domain is divided by a square mesh with $\Delta r = \Delta z = 0.02R_0$ or $\Delta r = \Delta z = 0.01R_0$. The increment of time Δt is taken to be 2.033×10^{-9} s for the coarse mesh. The increment of time for the fine mesh is shown later. Symmetric boundary conditions are used at the z axis. Non-reflection boundary conditions are applied to the top, left and right boundaries. The pressure behind the incident plane shock wave p_s is 1 GPa. The initial pressure around the bubble is p_0 ($= 100$ kPa) which is the same as the gas pressure inside the bubble and the glass pressure. The density of pre-shocked mercury is taken to be 13600 kg/m³. The density and velocity of post-shocked mercury are determined from the Rankine-Hugoniot jump condition. The Mach number of the incident shock wave is 1.068. The initial densities of air and glass are taken to be 1 kg/m³ and 2500 kg/m³, respectively. The initial velocities for pre-shocked mercury, air and glass are zero.

Figure 5 shows the pressure contours for mercury-air-glass systems. The successive bubble shapes after the impact of the liquid-jet on the downstream surface of the bubble are shown in Figure 6. The first and second rows in Figure 6 correspond to the bubble shapes calculated with a square mesh with $0.01R_0$ and $0.02R_0$, respectively. Figure 7 shows the influence of grid resolution on (a) bubble radius, (b) displacement of bubble centroid, (c) displacement of the center of glass surface, and (d) pressure at the center of glass surface. The bubble radius is defined as $R = (3V/4\pi)^{1/3}$ where V is a bubble volume. V is calculated with $V(t) = \int H(\varphi) dV$ where $H(\varphi)$ is a Heaviside function of the level set function as

$$H(\varphi) = \begin{cases} 1, & \varphi > 0, \\ 0, & \varphi < 0. \end{cases} \quad (13)$$

The displacement of bubble centroid is determined as $\delta z = z_b - z_b(t=0)$ where $z_b = \int_V z dV/V$. The displacement of the center of the glass surface is given by $\eta = z_g - z_g(t=0)$ where z_g is the location of the center of the glass surface in the z direction. The initial distance between the bubble centroid and the glass wall is taken to be $L/R_0 = 1.56$. The time indicated in the figures is non-dimensionalized by $t_0 = R_0/\sqrt{\Delta p/\rho_s}$ where $\Delta p = p_s - p_0$ and ρ_s is the density behind the incident shock wave. The increment of time for the fine mesh is taken to be $\Delta t = \Delta t_1 = 1.017 \times 10^{-9}$ s until the dimensionless time $t/t_0 = 1.281$. After the time, Δt is switched to $\Delta t = \Delta t_1/2$. Using the fine mesh makes the numerical stability severe because the finer surface structure is resolved with the finer mesh.

As shown in Figure 5(i), a strong expansion wave is produced in mercury when the incident shock impacts the bubble because the acoustic impedance of air is much lower than that of mercury. Since the acoustic impedance of glass is also lower than the mercury, an expansion wave reflects at the glass wall when the shock wave impacts the glass wall (Figure 5(ii, iii)). The difference of acoustic impedance between mercury and wall material is an important factor for cavitation inception; if the strong negative pressure reflects, cavitation may occur in mercury. After the expansion wave passes through the bubble, the pressure around the bubble decreases. As the bubble collapses, the surface of the glass wall is attracted to the bubble by the liquid flow induced by the bubble collapse (Figure 5(iv, v)). Then with

the increase of the liquid pressure at the upstream side of the bubble, the upstream surface deforms and the liquid-jet starts to form (Figure 5(v)). When the liquid-jet impacts the downstream surface of the bubble, a strong shock wave is generated at the point of jet impact (Figure 5(vi), Figure 6(i)). After the jet impacts the downstream surface, a thin gas layer is formed around the point of jet impact (Figure 6(ii)). As time goes by, the gas layer ahead the main bubble body spreads laterally due to the circulation flow around the bubble, which shows the clear vortex structure in Figure 6(iii, iv). Similar vortex structure was found in the experiments by Haas and Sturtevant [22]. When the bubble takes the minimum volume and rebounds, the rebounding shock wave is formed from the main body of the toroidal bubble (Figure 5(vii)). The rebounding shock wave focuses on the axis of symmetry, which leads to the high-pressure fields around the axis. Both the shock wave that occurs at the jet impact and the rebounding shock wave hit the glass wall (Figure 5(viii, ix)). After the shock waves impact the glass wall, the waves propagate in the glass. The impact of the strong shock waves leads to the formation of depression of the glass wall (Figure 5(x-xii), Figure 6(iii-v)). After the bubble volume takes a local maximum at about $t/t_0=1.7$ (Figure 5(xi)), the bubble collapses again. During the second collapse, the main body of the bubble penetrates into the depression of the glass wall (Figure 5(xii)). This can be a mechanism of cavitation erosion of the boundary. As shown in Futakawa et al. [4], the cavitation damage is predicted by the damage potential calculated from acoustic vibration caused by bubble collapse. The present simulation can provide the information about the displacement and velocity of glass wall needed to calculate the damage potential.

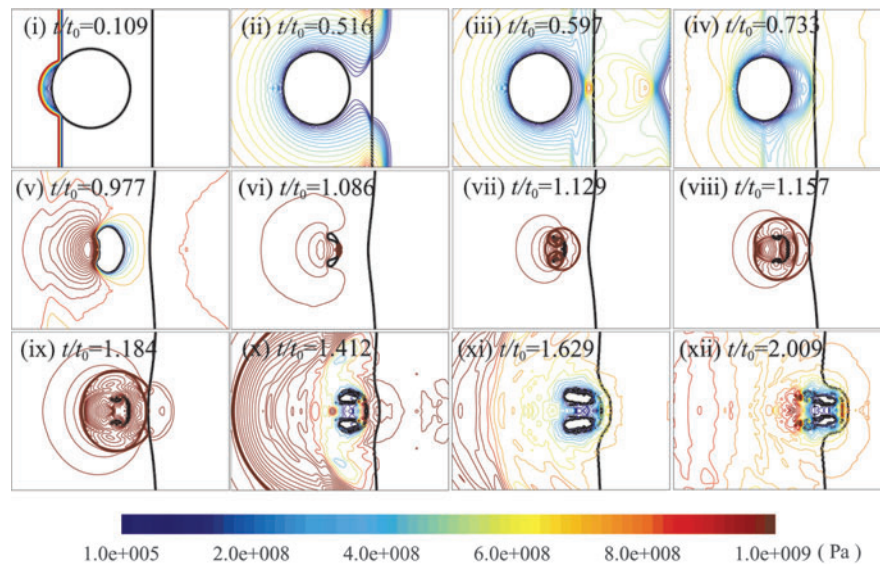


Figure 5. Pressure contours for bubble collapse near a glass wall ($L/R_0=1.56$).

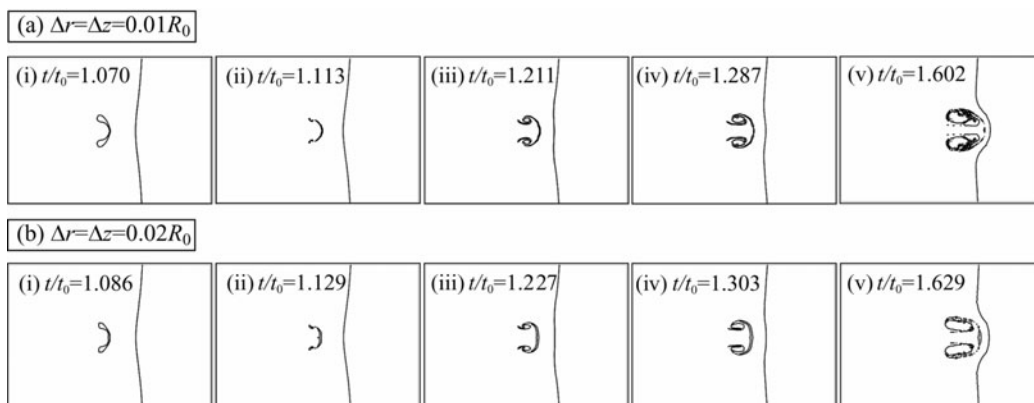


Figure 6. Success bubble shapes after jet impact: (a) $\Delta r = \Delta z = 0.01R_0$, (b) $\Delta r = \Delta z = 0.02R_0$.

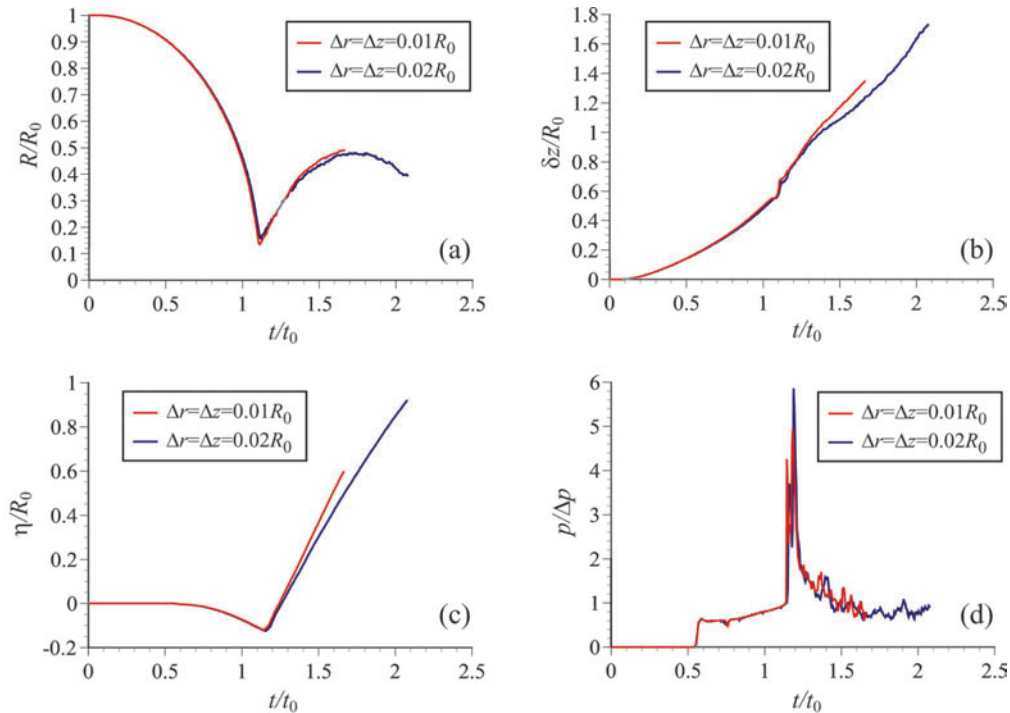


Figure 7. Influence of grid resolution on (a) bubble radius, (b) displacement of bubble centroid, (c) displacement of the center of glass surface, and (d) pressure at the center of glass surface.

The comparison of bubble shapes between Figures 6(a) and (b) shows that the detailed structure of the thin gas layer ahead the main body is dependent on the grid resolution. The finer the mesh becomes, the thinner the gas layer becomes. The fine mesh, therefore, is needed in order to discuss the detail of the formation and stability of the thin gas layer. Also, the displacements of the bubble centroid and the center of the glass surface after about $t/t_0 = 1.3$ are underestimated for the coarse mesh as shown in the Figure 7. This discrepancy is due to that the fine structure of gas-liquid interfaces is not resolved with the coarse mesh. However, the overall behaviors for the bubble radius, the displacement of bubble centroid, the displacement of the center of glass surface, and the pressure at the center of glass surface calculated with the $0.02R_0$ square mesh are in agreement with those with the $0.01R_0$ square mesh. The difference between the bubble radius at the time of jet impact calculated using the coarse mesh and that using the fine mesh is less than 7%. Thus the fundamental nature of bubble collapse near a glass wall in mercury can be discussed with the $0.02R_0$ square mesh. The detailed structure of the thin gas layer will be discussed in the future work.

The velocities at the north and south poles of the bubble surface and the velocity at the center of the glass surface are shown in Figure 8. After the jet impacts the downstream surface of the bubble, the velocities of the thin layer ahead the toroidal bubble are indicated in the figure. The velocity in the positive z direction is indicated by the positive sign. The velocity is non-dimensionalized by $\sqrt{\Delta p/\rho_s} = 267.05$ m/s. When the incident shock wave impacts the north pole, the velocity at the north pole, v_N , increases stepwisely. After the incident shock wave passes through the bubble, the high-pressure field is formed around the bubble. Since the pressure gradient at the bubble wall in the radial direction is positive, the pressure gradient induces the radial motion of the bubble. Therefore the velocity at the south pole becomes negative in the z direction. Since the pressure gradient is larger at the north pole, the velocity at the north pole becomes faster than that at the south pole, which causes the formation of liquid-jet. As time goes by, the bubble wall velocity is accelerated. Just before the jet impacts the downstream surface, v_N reaches about 1280 m/s; the Mach number is about 0.8. While, the velocity at the south pole, v_S , decreases as the bubble collapses. v_S just before the jet impact is about -280 m/s. Thus the Mach number of the relative velocity at the jet impact exceeds unity. After the jet impacts the downstream surface, the velocities at both sides of the thin gas layer decrease suddenly; v_N is almost the same as v_S . As shown in Figure 5, the rebounding shock wave is formed from the toroidal bubble.

The rebounding shock wave hits the thin gas layer ahead the main body, which results in the acceleration of the velocities at both sides of the layer at about $t/t_0 = 1.14$. On the other hand, when the bubble starts to collapse, the glass wall velocity v_g decreases due to the flow induced by the collapsing bubble. Then, when the shock wave that occurs at the jet impact hits the glass wall at about $t/t_0 = 1.16$, v_g rises dramatically. The impact of the rebounding shock wave at the glass wall also accelerates v_g .

Figure 9 shows the pressure contours for $L/R_0 = 1.06$ where the other initial conditions are the same as Figure 5. As the bubble collapses, the surface of the glass wall is attracted toward the bubble more strongly in Figure 9 than in Figure 5. As a result, the translation of the bubble is significantly reduced (see Figure 10(b)), and the surface instability (jet formation) occurs from both sides of the bubble. Such a bubble behavior is observed in the case of neutral bubble collapse [23, 24] because the acoustic impedance of glass is smaller than that of mercury. Finally, the bubble becomes a ring shape. The impulsive pressure at the center of glass surface for $L/R_0 = 1.06$ is higher than that for $L/R_0 = 1.56$. When $L/R_0 = 1.06$, the water hammer pressure evaluated with $\rho a v_{jet}$ where ρ is the density of mercury, a is the speed of sound in mercury, and v_{jet} is the liquid velocity just after the jet impacts the south pole of the bubble wall is $p/\Delta p = 20.1$, which is nearly the same as the maximum pressure at glass surface ($p/\Delta p = 17.8$) in Figure 10(d). The calculation is forced to stop because the number of grid points between the air-mercury and mercury-glass interfaces becomes one (see section 2.4.2).

Figure 10 shows the time histories of (a) bubble radius, (b) displacement of bubble centroid, (c) displacement of the center of the glass surface, and (d) pressure at the center of the glass surface for various distances between the bubble and the glass wall. The results for $L/R_0 = 1.06, 1.34, 1.56, 2.34,$

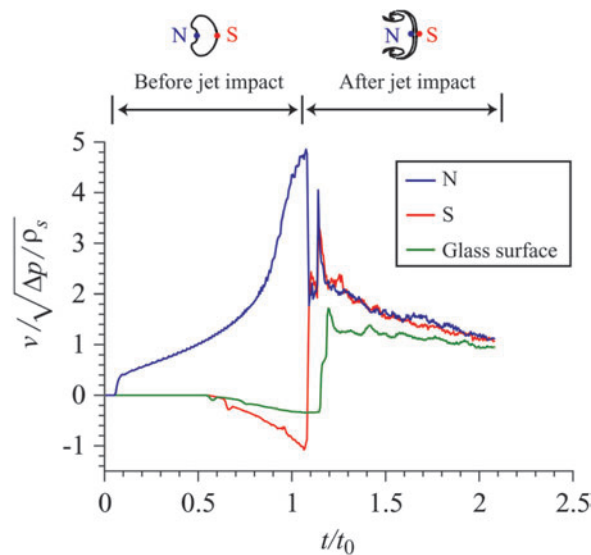


Figure 8. Velocity at north and south poles of bubble surface and the center of glass surface.

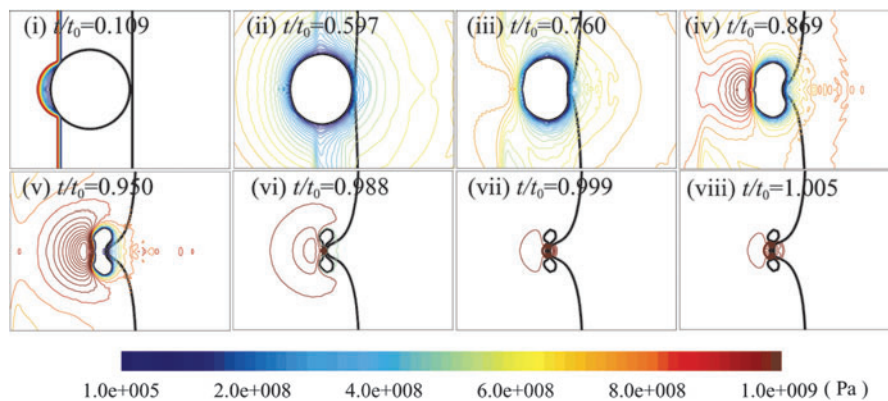


Figure 9. Pressure contours for bubble collapse near a glass wall ($L/R_0 = 1.06$).

Direct Numerical Simulations of Interaction of Strong Shock Waves with Nonspherical Gas Bubbles near Glass Boundaries in Mercury

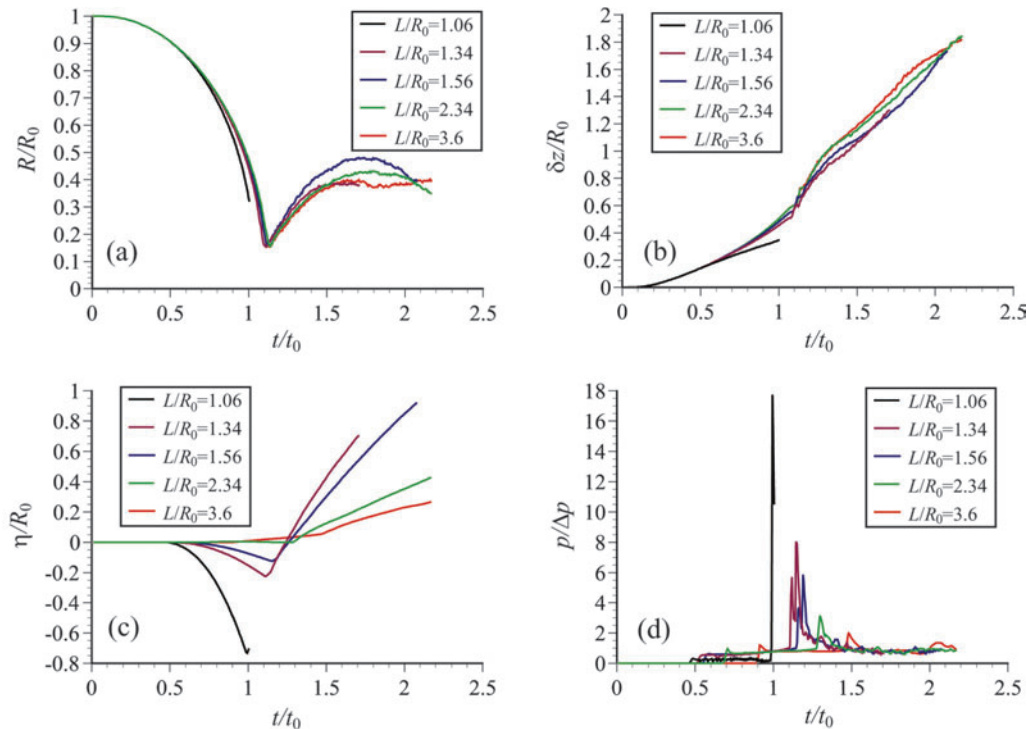


Figure 10. Time histories of (a) bubble radius, (b) displacement of bubble centroid, (c) displacement of the center of glass surface, and (d) pressure at the center of glass surface ($L/R_0 = 1.06, 1.34, 1.56, 2.34,$ and 3.6).

and 3.6 are indicated by black, purple, blue, green, and red lines, respectively. As shown in Figures 10(a) and (b), the time when the bubble rebounds becomes shorter and the displacement of bubble centroid becomes smaller as the distance between the bubble centroid and the glass wall becomes shorter: these results are caused by the deformation of the glass surface. As evident in Figure 10(c), the shorter the bubble-glass wall distance becomes, the more attracted the glass surface is toward the bubble during its collapse. When $L/R_0 = 2.34$ and 3.6 , the glass surface moves only in the positive z direction owing to the impact of the incident shock wave. Whether the glass surface is either attracted toward or repulsed from the bubble is dependent on L/R_0 . In the early stage of bubble collapse, the impact of the incident shock wave is a primary cause for the movement of the glass surface; the glass surface moves in the positive z direction. After the shock wave passes through the bubble, the positive pressure gradient in the radial direction is formed at the bubble wall. Thus, the bubble begins to collapse and the sink flow toward the bubble centroid is induced in the liquid. As the bubble collapse is accelerated, the sink flow becomes strong, which causes the attraction of glass surface toward the bubble. The velocity of the sink flow at the glass surface decreases with the increase of L/R_0 . Therefore, when L/R_0 is sufficiently large, the glass surface moves only in the positive z direction due to the impact of the incident shock wave. On the other hand, when L/R_0 is small, the glass surface is attracted toward the bubble because the influence of bubble collapse as a sink becomes prominent. After the liquid-jet impacts the bubble surface, the impulsive pressure by the shock waves generated from the bubble causes the movement of glass surface. Thus the glass surface always moves in the positive z direction after the liquid-jet impact.

These behaviors were observed in the collapse of a cylindrical bubble [7] and are similar to the bubble collapse near a compliant wall [23, 24]. As is well known, when the bubble collapses near a very light compliant wall, the bubble moves toward the opposite side of the compliant wall, and the liquid-jet occurs in the opposite direction to the compliant wall. For the moderate mass of the compliant wall, the neutral bubble collapse in which the bubble centroid is at rest is realized. Consequently, the bubble behavior in mercury near a glass wall is similar to that near a compliant wall; the translation of the bubble centroid toward the glass wall is suppressed and the collapse time becomes shorter. As shown in Figure 10(d), the double pressure peaks due to the shock wave that occurs at the liquid-jet impact

and the rebounding shock wave are observed in the pressure history when $L/R_0 = 1.34$ and 1.56 . The impact of the strong shock waves on the glass wall leads to the fast movement of the glass surface in the positive z direction in Figure 10(c).

We compare the present results with those for the 2D cylindrical bubbles by Takahira et al. [7]. Figure 11 shows the comparison of schlieren images when $L/R_0 = 1.56$. The numerical schlieren images are calculated with the same procedure as Ref. [25]. Also, the comparison of time histories of (a) bubble radius, (b) displacement of bubble centroid, (c) displacement of the center of the glass surface, and (d) pressure at the glass surface is shown in Figure 12. In Figure 12(a), the bubble radius R for the cylindrical bubble is evaluated by $R = \sqrt{V/\pi}$ where V is the two-dimensional bubble volume. As evident in Figure 12(a), the period of bubble collapse becomes shorter for the axi-symmetric bubble collapse. Consequently, the time when the liquid-jet impacts the downstream surface becomes shorter for the axi-symmetric bubble as shown in Figure 11. The bubble radius at the jet impact is smaller for

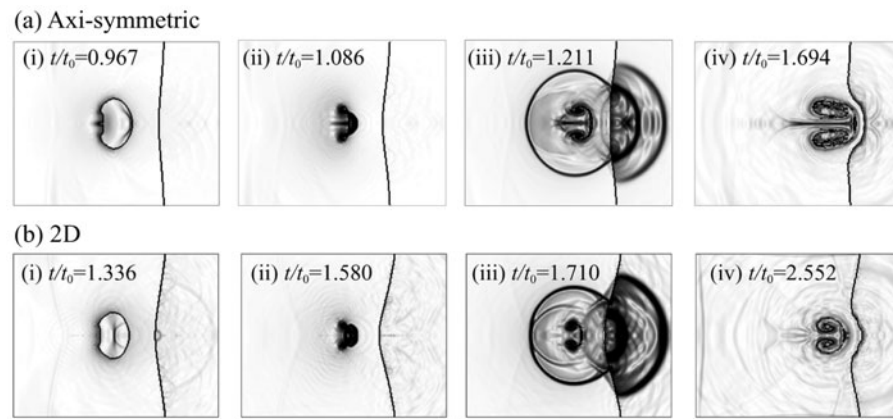


Figure 11. Comparison of schlieren images between (a) axi-symmetric bubble and (b) 2D cylindrical bubble [7] when $L/R_0 = 1.56$.

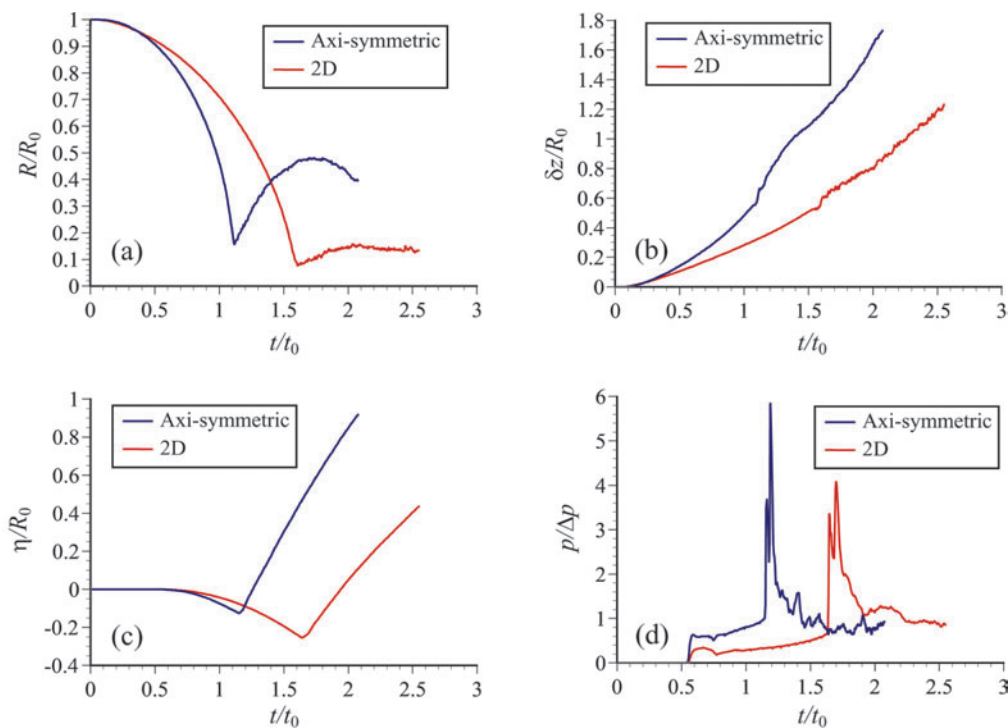


Figure 12. Comparison of (a) bubble radius, (b) displacement of bubble centroid, (c) displacement of the center of glass surface, and (d) pressure at the center of glass surface between axi-symmetric bubble and 2D cylindrical bubble [7] when $L/R_0 = 1.56$.

the cylindrical bubble. However, since the bubble wall velocity is faster for the axi-symmetric bubble, the impulsive pressure due to the impact of the liquid-jet on the downstream surface of the bubble is higher for the axi-symmetric bubble. Also, the higher rebounding shock wave is generated for the axi-symmetric bubble because the bubble volume becomes smaller. The translation of bubble centroid toward the glass wall is also accelerated for the axi-symmetric bubble. As a result, the glass wall is more affected by the collapse of bubbles; the higher impulsive pressure is observed at the glass wall and the depression of glass wall becomes deeper for the axi-symmetric bubble.

4. CONCLUSION

The axi-symmetric collapse of an initially spherical bubble induced by the shock-bubble interactions in mercury near a glass wall was investigated numerically. The improved Ghost Fluid Method (GFM), in which Riemann solutions were utilized to correct the values at boundary nodes, was applied to the present analysis. The mercury and glass were evaluated by using the equation of state for stiffened gas. The motions of three phases for air, mercury, and glass were solved directly coupling the GFM with the level set method.

The interaction of the incident shock wave with the bubble leads to the bubble deformation and the formation of liquid-jet during the collapse. Two kinds of strong shock waves are generated from the bubble in the mercury; one is the shock wave that occurs at the impact of the liquid-jet on the downstream surface of the bubble, and the other is rebounding shock wave. The focusing of the rebounding shock wave on the axis of symmetry results in the generation of local high-pressure region near the axis. It was shown that the impact of the shock waves leads to the formation of depression of the glass surface, and the toroidal bubble formed after the impact of liquid-jet penetrates into the depression. Thus, the present numerical method was applicable not only to the violent bubble collapse in mercury but also to the prediction of material damage; the shock waves produced by the bubble collapse cause the material damage.

The present results for the axi-symmetric bubble collapse were compared with those for the two-dimensional cylindrical bubble collapse in Ref. [7]. The results showed that the bubble takes a similar motion to that near a compliant wall in both two-dimensional and axi-symmetric collapses; the collapse time of a bubble becomes shorter than that of an isolated bubble; the translation of bubble centroid is reduced as the bubble-wall distance becomes shorter. However, the collapse time of the axi-symmetric bubble becomes shorter than that of the two-dimensional bubble; the bubble translation toward the glass wall becomes larger for the axi-symmetric bubble. The stronger shock waves are generated when the axi-symmetric bubble collapses, which results in the higher impulsive pressure at the glass wall and the deeper depression of the glass surface.

ACKNOWLEDGMENT

This work was partly supported by Grant-in-Aid for Scientific Research (No. 19560180) from JSPS.

REFERENCES

1. Brennen, C. E., *Cavitation and Bubble Dynamics*, Oxford University Press, Oxford, 1995.
2. Kodama, T. and Takayama, K., Dynamic Behavior of Bubbles during Extracorporeal Shock-Wave Lithotripsy, *Ultrasound in Med. & Biol.*, 1998, 24, 723-738.
3. Kodama, T., Hamblin, M. R. and Doukas, A. G., Cytoplasmic Molecular Delivery with Shock Wave: Importance of Impulse, *Biophys. J.*, 2000, 79, 1821-1832.
4. Futakawa, M. et al., Cavitation Erosion by Proton Beam Bombarding Mercury Target for Spallation Neutron Source -Damage Potential Evaluation by Measuring Acoustic Vibration-, *Proc. 6th Int. Symp. on Cavitation*, 2006, Total 6 pages.
5. Okita, K., Takagi, S. and Matsumoto, Y., Propagation of Pressure Waves, Caused by a Thermal Shock, in Liquid Metals Containing Gas Bubbles, *Journal of Fluid Science and Technology*, 3, 116-128.
6. Ida, M., Naoe, T. and Futakawa, M., Numerical Study of Gas and Cavitation Bubble Dynamics in Liquid Mercury under Negative Pressure, *Proc. 5th Joint ASME/JSME Fluids Eng. Conf.*, 2007, CD-ROM (No. FEDSM 2007-37297), Total 6 pages.
7. Takahira, H., Matsuno, T. and Shuto, K., Numerical Investigations of Shock-Bubble Interactions in Mercury, *Fluid Dynamics Research*, 2008, 40, 510-520.

8. Fedkiw, R., Aslam, T., Merriman, B. and Osher, S., A Non-Oscillatory Eulerian Approach to Interfaces in Multimaterial Flows (the Ghost Fluid Method), *J. Comput. Phys.*, 1999, 152, 457-492.
9. Fedkiw, R., Coupling an Eulerian Fluid Calculation to a Lagrangian Solid Calculation with the Ghost Fluid Method, *J. Comput. Phys.*, 2002, 175, 200-224.
10. Cocchi, J.-P. and Saurel, R., A Riemann Problem Based Method for the Resolution of Compressible Multimaterial Flows, *J. Comput. Phys.*, 1997, 137, 265-298.
11. Nourgaliev, R., Dinh, N. and Theofanous, T., Direct Numerical Simulation of Compressible Multiphase Flows: Interaction of Shock Waves with Dispersed Multimaterial Media, *Proc. 5th Int. Conf. on Multiphase Flow*, 2004, CD-ROM (Paper No.494), Total 18 pages.
12. Takahira, H. and Yuasa, S., Numerical Simulations of Shock-Bubble Interactions Using an Improved Ghost Fluid Method, *Proc. ASME Fluids Eng. Summer Meeting*, 2005, CD-ROM (No. FEDSM 2005-77119), Total 9 pages.
13. Takahira, H. and Yuasa, S., Investigations of Numerical Methods for Compressible Two-Phase Flows with the Ghost Fluid Method (2nd Report, Improvement for Gas-Liquid Two-Phase Flows), *Trans. Japan Soc. Mech. Eng.*, 2006, 72, 2643-2651 (in Japanese).
14. Saurel, R. and Abgrall, R., A Simple Method for Compressible Multifluid Flows, *SIAM J. Sci. Comput.*, 1999, 21, 1115-1145.
15. Zukas, J. A. Nicholas, T., Swift, H. F., Greszczuk, L. B. and Curran D. R., *Impact Dynamics*, John Wiley & Sons, New York, 1982.
16. Shu, C. -W. and Osher, S., Efficient Implementation of Essentially Non-Oscillatory Shock Capturing Schemes II, *J. Comput. Phys.*, 1989, 83, 32-78.
17. Sussman, M., Smereka, P. and Osher, S., A Level Set Approach for Computing Solutions to Incompressible Two-Phase Flow, *J. Comput. Phys.*, 1994, 114, 146-159.
18. Jiang, G. -S. and Peng, D., Weighted ENO Schemes for Hamilton-Jacobi Equations, *SIAM J. Sci. Comput.*, 2000, 21, 2126-2143.
19. Enright, D., Fedkiw, R., Ferziger, J. and Mitchell, I., A Hybrid Particle Level Set Method for Improved Interface Capturing., *J. Comput. Phys.*, 2002, 183, 83-116.
20. Adalsteinsson, D. and Sethian, J. A., The Fast Construction of Extension Velocities in Level Set Methods, *J. Comput. Phys.*, 1999, 148, 2-22.
21. Toro, E. F., *Riemann Solvers and Numerical Methods for Fluid Dynamics*, Springer-Verlag, Berlin, 1997.
22. Haas, J. -F. and Sturtevant, B., Interaction of Weak Shock Waves with Cylindrical and Spherical Gas Inhomogeneities, *J. Fluid Mech.*, 1987, 181, 41-76.
23. Shima, A., Tomita, Y., Gibson, D. C. and Blake, J. R., The Growth and Collapse of Cavitation Bubbles near Composite Surfaces, *J. Fluid Mech.*, 1989, 203, 199-214.
24. Duncan, J. H. and Zhang, S., On the Interaction of a Collapsing Cavity and a Compliant Wall, *J. Fluid Mech.*, 1991, 226, 401-423.
25. Quirk, J. J. and Karni, S., On the Dynamics of a Shock-Bubble Interaction, *J. Fluid Mech.*, 1996, 318, 129-163.

